Our results demonstrate that hybridization capture arrays can generate data from genomic target regions of megabase size from ancient DNA samples, even when only ~0.2% of the DNA in a sample stems from the endogenous genome. By generating an average coverage of 4- to 5-fold, errors from sequencing and small amounts of human DNA contamination can be minimized. A further approximately 5-fold reduction of errors was achieved here by the enzymatic removal of uracil residues that are frequent in ancient DNA (*25*). Because the Sidrón 1253 Neandertal library used for this study has been amplified and effectively immortalized, the same library should be able to provide similar-quality data for any other genomic target region, or even the entire single-copy fraction of the Neandertal genome.

References and Notes

1. R. E. Green *et al.*, *Science* **328**, 710 (2010).
2. H. N. Poinar *et al.*, *Science* **311**, 392 (2006).
3. W. Miller *et al.*, *Nature* **456**, 387 (2008).
4. A. W. Briggs *et al.*, *Science* **325**, 318 (2009).
5. J. Krause *et al.*, *Curr. Biol.* **20**, 231 (2010).
6. E. Hodges *et al.*, *Nat. Protoc.* **4**, 960 (2009).
7. E. Hodges *et al.*, *Nat. Genet.* **39**, 1522 (2007).
8. E. W. Sayers *et al.*, *Nucleic Acids Res.* **38** (Database issue), D5 (2010).
9. Materials and methods are available as supporting material on *Science* Online.
10. A. Rosas *et al.*, *Proc. Natl. Acad. Sci. U.S.A.* **103**, 19266 (2006).
11. T. De Torres *et al.*, *Archaeometry* 10.1111/j.1475-4754.2009.00491.x (2009).
12. H. M. Cann *et al.*, *Science* **296**, 261 (2002).
13. M. Meyer, M. Kircher, *Cold Spring Harb. Protoc.* 10.1101/pdb.prot5448 (2010).
14. R. E. Green *et al.*, *EMBO J.* **28**, 2494 (2009).
15. J. Krause *et al.*, *Curr. Biol.* **17**, 1908 (2007).
16. W. Enard *et al.*, *Nature* **418**, 869 (2002).
17. F. Vargha-Khadem, D. G. Gadian, A. Copp, M. Mishkin, *Nat. Rev. Neurosci.* **6**, 131 (2005).
18. K. Prüfer *et al.*, *BMC Bioinformatics* **8**, 41 (2007).
19. G. M. Cooper *et al.*, *Genome Res.* **15**, 901 (2005).
20. K. E. Lohmueller *et al.*, *Nature* **451**, 994 (2008).
21. B. Boeckmann *et al.*, *Nucleic Acids Res.* **31**, 365 (2003).
22. C. D. Bustamante *et al.*, *Nature* **437**, 1153 (2005).
23. H. H. Wu, B. Su, *BMC Evol. Biol.* **8**, 192 (2008).
24. J. M. Akey, *Genome Res.* **19**, 711 (2009).
25. A. W. Briggs *et al.*, *Nucleic Acids Res.* **38**, e87 (2010).

26. We thank C. S. Burbano, C. de Filippo, J. Kelso, and D. Reich for helpful comments; M. Kircher, K. Pruefer, and U. Stenzel for technical support; C. D. Bustamante and K. E. Lohmueller for access to human resequencing databases; D. L. Goode and A. Sidow for providing conservation scores; J. M. Akey for providing coordinates of genome-wide scans for selection; I. Gut for human genotyping; E. Leproust and M. Srinivasan for providing early access to the 1 Million feature Agilent microarrays; and the Genome Center at Washington University for pre-publication use of the orangutan genome assembly (http://genome.wustl.edu/genomes/view/pongo_abelii/). The government of the Principado de Asturias funded excavations at the Sidrón site. J.M.G. was supported by an NSF international postdoctoral fellowship (OISE-0754461) and E.H. by a postdoctoral training grant from the NIH and by a gift from the Stanley Foundation. G.J.H. is an investigator of the Howard Hughes Medical Institute, which together with the Presidential Innovation Fund of the Max Planck Society provided generous financial support. DNA sequences are deposited in the European Bioinformatics Institute short read archive, with accession number ERP000125. The array capture technologies used in this study are the subject of pending patent filings U.S. 60/478, 382 (filed 2003) and U.S. 61/205, 834 (filed 2009), on which G.J.H. and E.H. are listed as inventors.

Supporting Online Material
www.sciencemag.org/cgi/content/full/328/5979/723/DC1
Materials and Methods
Figs. S1 to S4
Tables S1 to S5

8 February 2010; accepted 1 April 2010
10.1126/science.1188046

Fermi Gamma-Ray Imaging of a Radio Galaxy

The Fermi-LAT Collaboration*†

The Fermi Gamma-ray Space Telescope has detected the γ-ray glow emanating from the giant radio lobes of the radio galaxy Centaurus A. The resolved γ-ray image shows the lobes clearly separated from the central active source. In contrast to all other active galaxies detected so far in high-energy γ-rays, the lobe flux constitutes a considerable portion (greater than one-half) of the total source emission. The γ-ray emission from the lobes is interpreted as inverse Compton–scattered relic radiation from the cosmic microwave background, with additional contribution at higher energies from the infrared-to-optical extragalactic background light. These measurements provide γ-ray constraints on the magnetic field and particle energy content in radio galaxy lobes, as well as a promising method to probe the cosmic relic photon fields.

Centaurus A (Cen A) is one of the brightest radio sources in the sky and was among the first identified with a galaxy (NGC 5128) outside of our Milky Way (*1*). Straddling the bright central source is a pair of extended radio lobes with a total angular extent of ~10° (*2*, *3*), which makes Cen A the largest discrete nonthermal extragalactic radio source visible from Earth. At a distance of 3.7 Mpc (*4*), it is the nearest radio galaxy to Earth, and the implied physical source size is ~600 kpc. Such double-lobed radio structures associated with otherwise apparently normal giant elliptical galaxies have become the defining feature of radio galaxies in general. The consensus explanation for this phenomenon is that the lobes are fueled by relativistic jets produced by accretion activity in a super-massive black hole residing at the galaxy's center.

With its unprecedented sensitivity and imaging capability (per-photon resolution: $\theta_{68} \simeq 0^{\circ}.8E_{\rm GeV}^{-0.8}$), the Fermi Large Area Telescope (LAT) (*5*) has detected and imaged the radio lobes of Cen A in high-energy γ-rays. The LAT image resulting from ~10 months of all-sky survey data (Fig. 1) clearly shows the γ-ray peak coincident with the active galactic nucleus detected by the Compton/EGRET instrument (*6*) and extended emission from the southern giant lobe. Because the northern lobe is characterized by lower surface-brightness emission (in radio), it is not immediately apparent from a naked-eye inspection of the γ-ray counts map. Nevertheless, from a counts profile extracted along the north-south axis of the source (Fig. 2), γ-ray excesses from both lobes are clearly visible.

Spectra for each of the lobes together with the central source (hereafter referred to as the "core") were determined with a binned maximum likelihood analysis implemented in GTLIKE (*7*) using events from 0.2 to 30 GeV in equal logarithmically spaced energy bins. We modeled background emission by including the Galactic diffuse component, an isotropic component, and nearby γ-ray point sources [see the supporting online material (SOM)]. We fit the core as a point source at the known radio position and modeled the lobe emission with a 22-GHz Wilkinson Microwave Anisotropy Probe (WMAP) image (Fig. 1) (*8*) with the core region within a 1° radius excluded as a spatial template. The modeled lobe region roughly corresponds to the regions 1 and 2 (north) and 4 and 5 (south) defined in (*9*), where region 3 is the core (Fig. 2). Assuming a power law for the γ-ray spectra, we find a large fraction (>1/2) of the total >100-MeV emission from Cen A to originate from the lobes with the flux in each of the northern $\{[0.77(+0.23/-0.19)_{\rm stat.}(\pm0.39)_{\rm syst.}] \times 10^{-7}\ {\rm ph\ cm^{-2}\ s^{-1}}\}$ and southern $\{[1.09(+0.24/-0.21)_{\rm stat.}(\pm0.32)_{\rm syst.}] \times 10^{-7}\ {\rm ph\ cm^{-2}\ s^{-1}}\}$ lobes smaller than the core flux $\{[1.50(+0.25/-0.22)_{\rm stat.}(\pm0.37)_{\rm syst.}] \times 10^{-7}\ {\rm ph\ cm^{-2}\ s^{-1}}\}$ (stat., statistical; syst., systematic). Uncertainties in the LAT effective area, the Galactic diffuse model used, and the core exclusion region were considered to be sources of systematic error (SOM). The resultant test statistic (*10*) for the northern and southern giant lobes are 29 and 69, which correspond to detection significances of 5.0σ and 8.0σ, respectively. The lobe spectra are steep, with photon indices $\Gamma = 2.52(+0.16/-0.19)_{\rm stat.}(\pm0.25)_{\rm syst.}$ (north) and $2.60(+0.14/-0.15)_{\rm stat.}(\pm0.20)_{\rm syst.}$ (south) in which photons up to ~2 to 3 GeV are currently detected. These values are consistent with that of the core [$\Gamma = 2.67(\pm0.10)_{\rm stat.}(\pm0.08)_{\rm syst.}$], which

*All authors with their affiliations appear at the end of this paper.
†To whom correspondence should be addressed. E-mail: Teddy.Cheung.ctr@nrl.navy.mil (C.C.C.); fukazawa@hep01.hepl.hiroshima-u.ac.jp (Y.F.); jurgen.knodlseder@cesr.fr (J.K.); stawarz@slac.stanford.edu (Ł.S.)

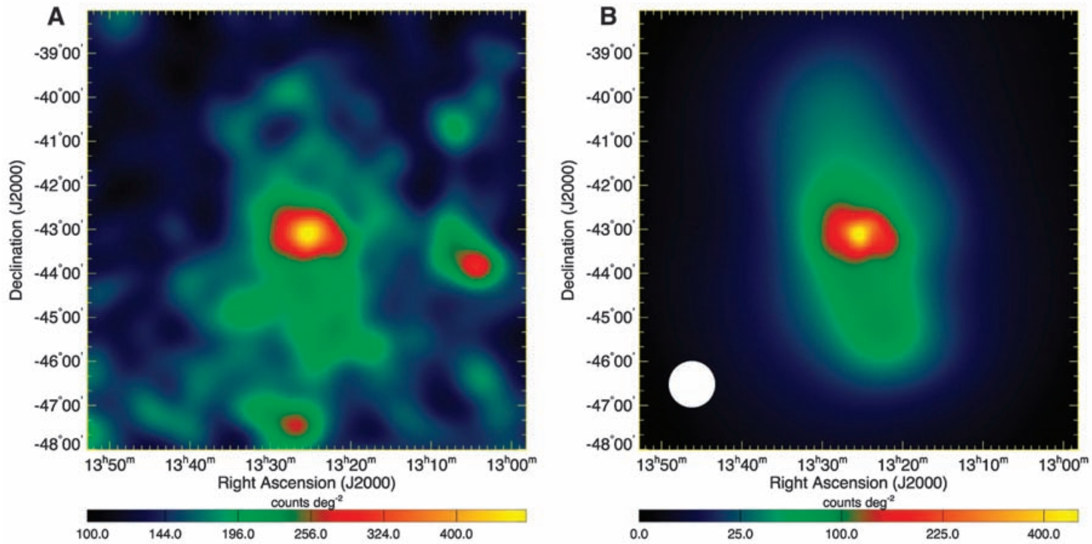

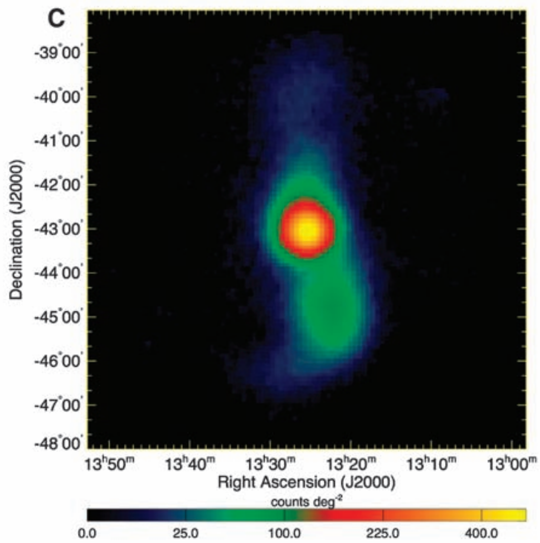

Fig. 1. (**A** and **B**) Fermi-LAT γ-ray (>200 MeV) counts maps centered on Cen A, displayed with square-root scaling. In both (A) and (B), models of the galactic and isotropic emission components were subtracted from the data (in contrast to the observed counts profile presented in Fig. 2). The images are shown before (A) and after (B) additional subtraction of field point sources (SOM) and are shown adaptively smoothed with a minimum signal-to-noise ratio of 10. In (B), the white circle with a diameter of 1° is approximately the scale of the LAT point-spread function width. (**C**) For comparison, the 22-GHz radio map from the 5-year WMAP data set (*8*) with a resolution of 0°.83 is shown. J2000, equinox; h, hour; m, minutes.

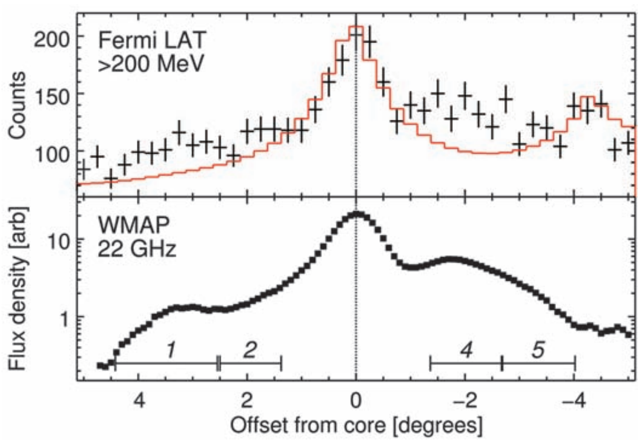

Fig. 2. Observed intensity profiles of Cen A along the north-south axis in γ-rays (**top**) and in the radio band (**bottom**). In the bottom panel, the lobe regions 1 and 2 (northern lobe) and regions 4 and 5 (southern lobe) are indicated as in (*9*), where region 3 (not displayed here) is the core. The red curve overlaid onto the LAT data indicates the emission model for all fitted points sources, plus the isotropic and Galactic diffuse (brighter to the south) emission. The point sources include the Cen A core (offset = 0°) and a LAT source (offset = −4.5°) (see SOM) that is clearly outside (1° from the southern edge) of the southern lobe. The excess counts are coincident with the northern and southern giant lobes. arb, arbitrary units.

is known to have a steep γ-ray spectrum (*6*). For further details pertaining to the analysis of the lobe emission, see the SOM.

It is well-established that radio galaxy lobes are filled with magnetized plasma containing ultra-relativistic electrons emitting synchrotron radiation in the radio band (observed frequencies: $\nu \sim 10^7$ to 10^{11} Hz). These electrons also up-scatter ambient photons to higher energies via the inverse Compton (IC) process. At the observed distances far from the parent galaxy (>100-kpc scale), the dominant soft-photon field surrounding the extended lobes is the pervading radiation from the cosmic microwave background (CMB) (*11*). Because IC/CMB scattered emission in the lobes of more distant radio galaxies is generally well observed in the x-ray band (*12*–*14*), the IC spectrum can be expected to extend to even higher energies (*9*, *15*), as demonstrated by the LAT detection of the Cen A giant lobes.

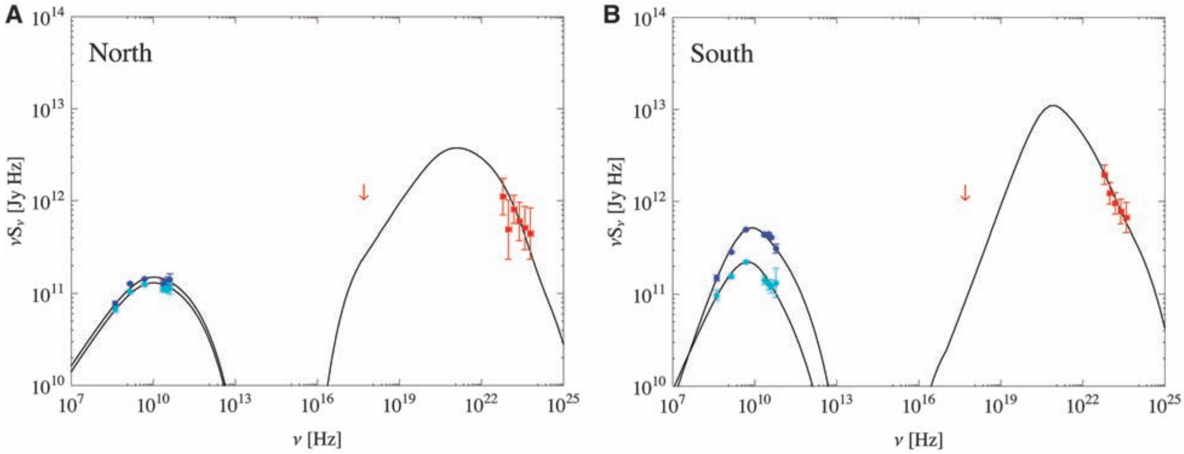

Fig. 3. Broad-band SEDs of the northern (**A**) and southern (**B**) giant lobes of Cen A. The radio measurements (up to 60 GHz) of each lobe are separated into two regions, with dark blue data points indicating regions that are closer to the nucleus (regions 2 and 4; see Fig. 2), and light blue points denoting the farther regions (1 and 5). Synchrotron continuum models for each region are overlaid. The component at higher energies is the total IC emission of each lobe modeled to match the LAT measurements (red points with error bars; error bars indicate 1 σ errors). The x-ray limit for the lobe emission derived from *SAS*-3 observations (*24*) is indicated with a red arrow [see (*9*)]. The break and maximum frequencies in the synchrotron spectra are ν_{br} = 4.8 GHz and ν_{max} = 400 GHz, respectively. νS_ν, frequency multiplied by flux density.

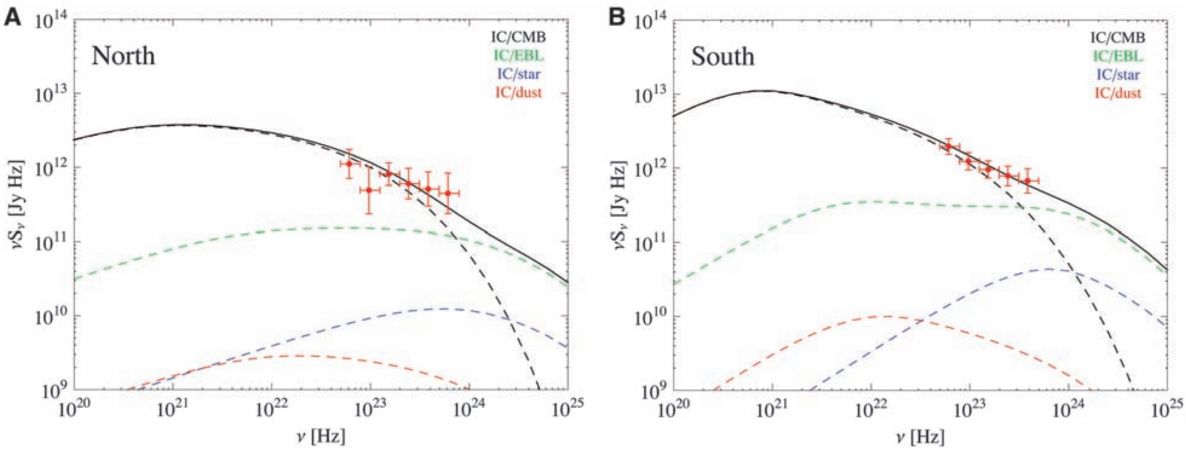

Fig. 4. Detail of the IC portion of the northern (**A**) and southern (**B**) giant lobes' SEDs (Fig. 3). The separate contributions from the different photon seed sources are indicated with dashed lines, and the total emission is represented by the solid black line. Red data points and error bars are the same as in Fig. 3. Vertical bars indicate errors; horizontal bars indicate frequency range.

To model the observed lobe γ-rays as IC emission, detailed radio measurements of the lobes' synchrotron continuum spectra are necessary to infer the underlying electron energy distribution (EED), $n_e(\gamma)$, where the electron energy is $E_e = \gamma m_e c^2$ (γ, electron Lorentz factor; m_e, electron mass; c, speed of light; n_e, number density of electrons). In anticipation of these Fermi observations, ground-based (*16*, *17*) and WMAP satellite (*8*) maps of Cen A were previously analyzed (*9*). Here, we separately fit the 0.4- to 60-GHz measurements for each region defined therein for the north (1 and 2) and south (4 and 5) lobes (Fig. 2) with EEDs in the form of a broken power law (with normalization k_e and slopes s_1 and s_2) plus an exponential cutoff at high energies $n_e(\gamma) = k_e\gamma^{-s_1}$ for $\gamma_{min} \leq \gamma < \gamma_{br}$ and $n_e(\gamma) = k_e\gamma_{br}^{s_2-s_1}\gamma^{-s_2}\exp[-\gamma/\gamma_{max}]$ for $\gamma \geq \gamma_{br}$, such that the electron energy density is $U_e = \int E_e n_e(\gamma)d\gamma$. To a certain extent, our modeling results depend on the shape of the electron spectrum at energies higher than those probed by the WMAP measurements ($\nu \gtrsim$ 60 GHz) (Fig. 3); we have assumed the spectrum to decline exponentially.

We calculated the IC spectra resulting from the fitted EED (parameters listed in table S1 of the SOM) by employing precise synchrotron (*18*) and IC (*19*) kernels (including Klein-Nishina effects) by adjusting the magnetic field B. In addition to the CMB photons, we included IC emission off the isotropic infrared-to-optical extragalactic background light (EBL) radiation field (*9*, *20*, *21*), using the data compilation from (*22*). Anisotropic radiation from the host galaxy starlight and the well-known dust lane was also included, but was found to have a negligible contribution in comparison to the EBL (Fig. 4 and SOM). The resultant total IC spectra of the northern and southern lobes (Fig. 3) with B = 0.89 μG (north) and 0.85 μG (south) provide satisfactory representations of the observed γ-ray data. These B-field values imply that the high-energy γ-ray emission detected by the LAT is dominated by the scattered CMB emission, with the EBL contributing at higher energies ($\gtrsim$1 GeV) (Fig. 4).

Considering only contributions from ultra-relativistic electrons and magnetic field, the lobe plasma is found to be close to the minimum-energy condition with the ratio of the energy densities $U_e/U_B \simeq 4.3$ (north) and $\simeq 1.8$ (south), where $U_B = B^2/8\pi$. The EED was assumed to extend down to $\gamma_{min} = 1$; adopting larger values can reduce this ratio by a fractional amount for the southern lobe and by up to ~two times for the northern lobe (SOM). For comparison, IC/CMB x-ray measurements of extended lobes of more powerful [Fanaroff-Riley type-II (*23*)] radio sources have been used to infer higher B fields and equipartition ratios with a range $U_e/U_B \simeq 1{-}10$ (*12*–*14*).

The radiating particles in the Cen A lobes lose energy predominantly through the IC channel, because the ratio of the corresponding cooling times is equal to the energy density ratio $U_{\rm CMB}/U_{\rm B} \gtrsim 10$. This manifests itself in the approximately one order of magnitude dominance of the γ-ray component over the radio component in the observed spectral energy distributions (SEDs) (Fig. 3). However, the magnetic-field constraints (thus, the exact ratios of $U_{\rm CMB}/U_{\rm B}$) are sensitive to the shape of the EED at the electron energies $E_{\rm e} > 0.1$ TeV. On one hand, magnetic-field strengths greater than $B \sim 1$ μG will underproduce the observed LAT emission for all reasonable forms of the EED, so the quoted ratio is formally a lower limit. Conversely, magnetic fields as low as ~one-third of our quoted values are strictly allowed if we invoke a sharper cutoff in the synchrotron spectrum at $\gtrsim 60$ GHz, as would be expected in some aging models for extended radio lobes (*9*). Such models with lower magnetic fields and EEDs with sharper upper-energy cutoffs than the exponential form adopted here (Fig. 3) would result in IC spectra in which the EBL, rather than the CMB, component becomes dominant in the LAT observing band. These models require large departures from equipartition ($U_{\rm e}/U_{\rm B} \gtrsim 10$); even lower B fields would violate the observed x-ray limit to the lobe flux (*9*, *24*).

For a tangled magnetic field, the total nonthermal pressures in the lobes are $p_{\rm rel} = (U_{\rm e} + U_{\rm B})/3 \simeq 5.6 \times 10^{-14}$ erg cm^{-3} (north) and $\simeq 2.7 \times 10^{-14}$ erg cm^{-3} (south). Such estimates can be compared to the ambient thermal gas pressure to enable further understanding of the dynamical evolution of such giant structures in general. Unfortunately, the parameters of the thermal gas at the appropriate distances from the nucleus of Cen A are not well known. Upper limits of the soft x-ray emission of the lobes (*9*), as well as Faraday rotation studies (*25*), indicate that the thermal gas number density is $n_{\rm gas} < 10^{-4}$ cm^{-3} within the giant lobes. Hence, the upper limit for the thermal pressure $p_{\rm gas} = nkT < 10^{-13}(n_{\rm gas}/10^{-4}\ {\rm cm}^{-3})(T_{\rm gas}/10^{7}\ {\rm K})$ erg cm^{-3} (k, the Boltzmann constant; T, temperature) is comparable to the evaluated nonthermal pressures.

Our modeling results allow us to estimate the total energy in both giant lobes $E_{\rm tot}$ 1.5×10^{58} erg. This energy, divided by the lifetime of the lobes derived from spectral aging $\tau \simeq 3\times 10^{7}$ years (*9*), gives the required kinetic power of the jets inflating the giant lobes, $L_{\rm j} \simeq E_{\rm tot}/2\tau \simeq 7.7 \times 10^{42}$ erg s^{-1}, which is close to the estimates of the total power of the kiloparsec-scale outflow in the current epoch of jet activity (*26*). For a black hole mass in Cen A, $M_{\rm BH} \simeq 10^{8} M_{\odot}$ ($M_{\odot}$, mass of the sun) (*27*), this implies a jet power that is only a small fraction of the Eddington luminosity ($L_{\rm j} \simeq 6.1 \times 10^{-4} L_{\rm Edd}$), as well as a relatively small jet production efficiency ($E_{\rm tot}/M_{\rm BH}c^{2} \simeq 8 \times 10^{-5}$). Because the work done by the expanding lobes on the ambient medium is not taken into account and the relativistic proton content is unconstrained in our analysis, the obtained values for $E_{\rm tot}$ and $L_{\rm j}$ are strict lower limits and could plausibly be an order of magnitude larger (*28*).

The observed LAT emission implies the presence of 0.1 to 1 TeV electrons in the few hundred kiloparsec–scale lobes. Because their radiative lifetimes (<1 to 10 million years) approach plausible electron transport time scales across the lobes, the particles have been either accelerated in situ or efficiently transported from regions closer to the nucleus. Such high-energy electrons in the lobes are, in fact, required to IC scatter photons into the LAT band, and it is presently unclear how common this is in other radio galaxies.

References and Notes

1. J. G. Bolton, G. J. Stanley, O. B. Slee, *Nature* **164**, 101 (1949).
2. C. A. Shain, *Aust. J. Phys.* **11**, 517 (1958).
3. K. V. Sheridan, *Aust. J. Phys.* **11**, 400 (1958).
4. L. Ferrarese *et al.*, *Astrophys. J.* **654**, 186 (2007).
5. W. B. Atwood *et al.*, *Astrophys. J.* **697**, 1071 (2009).
6. R. C. Hartman *et al.*, *Astrophys. J. Suppl. Ser.* **123**, 79 (1999).
7. http://fermi.gsfc.nasa.gov/ssc/data/analysis/documentation/Cicerone/
8. G. Hinshaw *et al.*, *Astrophys. J. Suppl. Ser.* **180**, 225 (2009).
9. M. J. Hardcastle, C. C. Cheung, I. J. Feain, Ł. Stawarz, *Mon. Not. R. Astron. Soc.* **393**, 1041 (2009).
10. J. R. Mattox *et al.*, *Astrophys. J.* **461**, 396 (1996).
11. D. E. Harris, J. E. Grindlay, *Mon. Not. R. Astron. Soc.* **188**, 25 (1979).
12. E. D. Feigelson, S. A. Laurent-Muehleisen, R. I. Kollgaard, E. B. Fomalont, *Astrophys. J.* **449**, L149 (1995).
13. J. H. Croston *et al.*, *Astrophys. J.* **626**, 733 (2005).
14. J. Kataoka, Ł. Stawarz, *Astrophys. J.* **622**, 797 (2005).
15. C. C. Cheung, *AIP Conf. Ser.* **921**, 325 (2007).
16. N. Junkes, R. F. Haynes, J. I. Harnett, D. L. Jauncey, *Astron. Astrophys.* **269**, 29 (1993).
17. H. Alvarez, J. Aparici, J. May, P. Reich, *Astron. Astrophys.* **355**, 863 (2000).
18. A. Crusius, R. Schlickeiser, *Astron. Astrophys.* **164**, L16 (1986).
19. G. R. Blumenthal, R. J. Gould, *Rev. Mod. Phys.* **42**, 237 (1970).
20. M. G. Hauser, E. Dwek, *Annu. Rev. Astron. Astrophys.* **39**, 249 (2001).
21. M. Georganopoulos *et al.*, *Astrophys. J.* **686**, L5 (2008).
22. M. Raue, D. Mazin, *Int. J. Mod. Phys. D* **17**, 1515 (2008).
23. B. L. Fanaroff, J. M. Riley, *Mon. Not. R. Astron. Soc.* **167**, 31P (1974).
24. F. J. Marshall, G. W. Clark, *Astrophys. J.* **245**, 840 (1981).
25. I. J. Feain *et al.*, *Astrophys. J.* **707**, 114 (2009).
26. J. H. Croston *et al.*, *Mon. Not. R. Astron. Soc.* **395**, 1999 (2009).
27. A. Marconi *et al.*, *Astron. Astrophys.* **448**, 921 (2006).
28. C. D. Dermer, S. Razzaque, J. D. Finke, A. Atoyan, *N. J. Phys.* **11**, 065016 (2009).

29. The Fermi-LAT Collaboration acknowledges support from a number of agencies and institutes for both the development and operation of the LAT, as well as for scientific data analysis. These organizations include NASA and the U.S. Department of Energy in the United States; Commissariat à l'Energie Atomique and the Centre National de la Recherche Scientifique/Institut National de Physique Nucléaire et de Physique des Particules in France; the Agenzia Spaziale Italiana and the Istituto Nazionale de Fisica Nucleare in Italy; the Ministry of Education, Culture, Sports, Science and Technology (MEXT), High Energy Accelerator Research Organization (KEK), and Japan Aerospace Exploration Agency (JAXA) in Japan; and the K. A. Wallenberg Foundation, the Swedish Research Council, and the National Space Board in Sweden. Additional support from Istituto Nazionale di Astrofisica in Italy and Centre National d'Études Spatiales in France for science analysis during the operations phase is also gratefully acknowledged. C.C.C. was supported by the NASA Postdoctoral Program at Goddard Space Flight Center, administered by Oak Ridge Associated Universities through a contract with NASA. J. Conrad is a Royal Swedish Academy of Sciences research fellow (funded by a grant from the K. A. Wallenberg Foundation). We thank N. Odegard for providing the WMAP image.

The Fermi-LAT Collaboration

A. A. Abdo,[1,2] M. Ackermann,[3] M. Ajello,[3] W. B. Atwood,[4] L. Baldini,[5] J. Ballet,[6] G. Barbiellini,[7,8] D. Bastieri,[9,10] B. M. Baughman,[11] K. Bechtol,[3] R. Bellazzini,[5] B. Berenji,[3] R. D. Blandford,[3] E. D. Bloom,[3] E. Bonamente,[12,13] A. W. Borgland,[3] J. Bregeon,[5] A. Brez,[5] M. Brigida,[14,15] P. Bruel,[16] T. H. Burnett,[17] S. Buson,[10] G. A. Caliandro,[18] R. A. Cameron,[3] P. A. Caraveo,[19] J. M. Casandjian,[6] E. Cavazzuti,[20] C. Cecchi,[12,13] Ö. Çelik,[21,22,23] A. Chekhtman,[1,24] C. C. Cheung,[1,2,21]† J. Chiang,[3] S. Ciprini,[13] R. Claus,[3] J. Cohen-Tanugi,[25] S. Colafrancesco,[20] L. R. Cominsky,[26] J. Conrad,[27,28] L. Costamante,[3] S. Cutini,[20] D. S. Davis,[21,23] C. D. Dermer,[1] A. de Angelis,[29] F. de Palma,[14,15] S. W. Digel,[3] E. do Couto e Silva,[3] P. S. Drell,[3] R. Dubois,[3] D. Dumora,[30,31] C. Farnier,[25] C. Favuzzi,[14,15] S. J. Fegan,[16] J. Finke,[1,2] W. B. Focke,[3] P. Fortin,[16] Y. Fukazawa,[32]† S. Funk,[3] P. Fusco,[14,15] F. Gargano,[15] D. Gasparrini,[20] N. Gehrels,[21,33,34] M. Georganopoulos,[23] S. Germani,[12,13] B. Giebels,[16] N. Giglietto,[14,15] F. Giordano,[14,15] M. Giroletti,[35] T. Glanzman,[3] G. Godfrey,[3] I. A. Grenier,[6] J. E. Grove,[1] L. Guillemot,[36] S. Guiriec,[37] Y. Hanabata,[32] A. K. Harding,[21] M. Hayashida,[3] E. Hays,[21] R. E. Hughes,[11] M. S. Jackson,[28,38] G. Jóhannesson,[3] A. S. Johnson,[3] T. J. Johnson,[21,34] W. N. Johnson,[1] T. Kamae,[3] H. Katagiri,[32] J. Kataoka,[39] N. Kawai,[40,41] M. Kerr,[17] J. Knödlseder,[42]† M. L. Kocian,[3] M. Kuss,[5] J. Lande,[3] L. Latronico,[5] M. Lemoine-Goumard,[30,31] F. Longo,[7,8] F. Loparco,[14,15] B. Lott,[30,31] M. N. Lovellette,[1] P. Lubrano,[12,13] G. M. Madejski,[3] A. Makeev,[1,24] M. N. Mazziotta,[15] W. McConville,[21,34] J. E. McEnery,[21,34] C. Meurer,[27,28] P. F. Michelson,[3] W. Mitthumsiri,[3] T. Mizuno,[32] A. A. Moiseev,[22,34] C. Monte,[14,15] M. E. Monzani,[3] A. Morselli,[43] I. V. Moskalenko,[3] S. Murgia,[3] P. L. Nolan,[3] J. P. Norris,[44] E. Nuss,[25] T. Ohsugi,[32] N. Omodei,[5] E. Orlando,[45] J. F. Ormes,[44] D. Paneque,[3] D. Parent,[30,31] V. Pelassa,[25] M. Pepe,[12,13] M. Pesce-Rollins,[5] F. Piron,[25] T. A. Porter,[4] S. Rainò,[14,15] R. Rando,[9,10] M. Razzano,[5] S. Razzaque,[1,2] A. Reimer,[3,46] O. Reimer,[3,46] T. Reposeur,[30,31] S. Ritz,[4] L. S. Rochester,[3] A. Y. Rodriguez,[18] R. W. Romani,[3] M. Roth,[17] F. Ryde,[28,38] H. F.-W. Sadrozinski,[4] R. Sambruna,[21] D. Sanchez,[16] A. Sander,[11] P. M. Saz Parkinson,[4] J. D. Scargle,[47] C. Sgrò,[5] E. J. Siskind,[48] D. A. Smith,[30,31] P. D. Smith,[11] G. Spandre,[5] P. Spinelli,[14,15] J.-L. Starck,[6] Ł. Stawarz,[3,49]† M. S. Strickman,[1] D. J. Suson,[50] H. Tajima,[3] H. Takahashi,[32] T. Takahashi,[51] T. Tanaka,[3] J. B. Thayer,[3] J. G. Thayer,[3] D. J. Thompson,[21] L. Tibaldo,[6,9,10] D. F. Torres,[18,52] G. Tosti,[12,13] A. Tramacere,[3,53] Y. Uchiyama,[3] T. L. Usher,[3] V. Vasileiou,[22,23] N. Vilchez,[42] V. Vitale,[43,54] A. P. Waite,[3] E. Wallace,[17] P. Wang,[3] B. L. Winer,[11] K. S. Wood,[1] T. Ylinen,[28,38,55] M. Ziegler,[4] M. J. Hardcastle,[56] D. Kazanas[21]

[1]Space Science Division, Naval Research Laboratory, Washington, DC 20375, USA. [2]National Research Council Research Associate, National Academy of Sciences, Washington, DC 20001, USA. [3]W. W. Hansen Experimental Physics Laboratory, Kavli Institute for Particle Astrophysics and Cosmology, Department of Physics and SLAC National Accelerator Laboratory, Stanford University, Stanford, CA 94305, USA. [4]Santa Cruz Institute for Particle Physics, Department of Physics and Department of Astronomy and Astrophysics, University of California at Santa Cruz, Santa Cruz, CA 95064, USA. [5]Istituto Nazionale di Fisica Nucleare, Sezione di Pisa, I-56127 Pisa, Italy. [6]Laboratoire AIM, CEA-IRFU/CNRS/Université Paris Diderot, Service d'Astrophysique, CEA Saclay, 91191 Gif sur Yvette, France. [7]Istituto Nazionale di Fisica Nucleare, Sezione di Trieste, I-34127 Trieste, Italy. [8]Dipartimento di Fisica, Università di Trieste, I-34127 Trieste, Italy. [9]Istituto Nazionale di Fisica Nucleare, Sezione di Padova, I-35131 Padova, Italy. [10]Dipartimento di Fisica "G. Galilei," Università di Padova, I-35131 Padova, Italy. [11]Department of Physics, Center for Cosmology and Astro-Particle Physics, The Ohio State University, Columbus, OH

43210, USA. [12]Istituto Nazionale di Fisica Nucleare, Sezione di Perugia, I-06123 Perugia, Italy. [13]Dipartimento di Fisica, Università degli Studi di Perugia, I-06123 Perugia, Italy. [14]Dipartimento di Fisica "M. Merlin" dell'Università e del Politecnico di Bari, I-70126 Bari, Italy. [15]Istituto Nazionale di Fisica Nucleare, Sezione di Bari, 70126 Bari, Italy. [16]Laboratoire Leprince-Ringuet, École polytechnique, CNRS/IN2P3, Palaiseau, France. [17]Department of Physics, University of Washington, Seattle, WA 98195–1560, USA. [18]Institut de Ciencies de l'Espai (IEEC-CSIC), Campus UAB, 08193 Barcelona, Spain. [19]Istituto Nazionale di Astrofisica (INAF)–Istituto di Astrofisica Spaziale e Fisica Cosmica, I-20133 Milano, Italy. [20]Agenzia Spaziale Italiana Science Data Center, I-00044 Frascati (Roma), Italy. [21]NASA Goddard Space Flight Center, Greenbelt, MD 20771, USA. [22]Center for Research and Exploration in Space Science and Technology and NASA Goddard Space Flight Center, Greenbelt, MD 20771, USA. [23]Department of Physics and Center for Space Sciences and Technology, University of Maryland Baltimore County, Baltimore, MD 21250, USA. [24]George Mason University, Fairfax, VA 22030, USA. [25]Laboratoire de Physique Théorique et Astroparticules, Université Montpellier 2, CNRS/IN2P3, Montpellier, France. [26]Department of Physics and Astronomy, Sonoma State University, Rohnert Park, CA 94928–3609, USA. [27]Department of Physics, Stockholm University, AlbaNova, SE-106 91 Stockholm, Sweden. [28]The Oskar Klein Centre for Cosmoparticle Physics, AlbaNova, SE-106 91 Stockholm, Sweden. [29]Dipartimento di Fisica, Università di Udine and Istituto Nazionale di Fisica Nucleare, Sezione di Trieste, Gruppo Collegato di Udine, I-33100 Udine, Italy. [30]Université de Bordeaux, Centre d'Études Nucléaires Bordeaux Gradignan, UMR 5797, Gradignan, 33175, France. [31]CNRS/IN2P3, Centre d'Études Nucléaires Bordeaux Gradignan, UMR 5797, Gradignan, 33175, France. [32]Department of Physical Sciences, Hiroshima University, Higashi-Hiroshima, Hiroshima 739-8526, Japan. [33]Department of Astronomy and Astrophysics, Pennsylvania State University, University Park, PA 16802, USA. [34]Department of Physics and Department of Astronomy, University of Maryland, College Park, MD 20742, USA. [35]INAF Istituto di Radioastronomia, 40129 Bologna, Italy. [36]Max-Planck-Institut für Radioastronomie, Auf dem Hügel 69, 53121 Bonn, Germany. [37]Center for Space Plasma and Aeronomic Research, University of Alabama in Huntsville, Huntsville, AL 35899, USA. [38]Department of Physics, Royal Institute of Technology, AlbaNova, SE-106 91 Stockholm, Sweden. [39]Waseda University, 1-104 Totsukamachi, Shinjuku-ku, Tokyo, 169-8050, Japan. [40]Department of Physics, Tokyo Institute of Technology, Meguro City, Tokyo 152-8551, Japan. [41]Cosmic Radiation Laboratory, Institute of Physical and Chemical Research (RIKEN), Wako, Saitama 351-0198, Japan. [42]Centre d'Étude Spatiale des Rayonnements, CNRS/UPS, BP 44346, F-30128 Toulouse Cedex 4, France. [43]Istituto Nazionale di Fisica Nucleare, Sezione di Roma "Tor Vergata," I-00133 Roma, Italy. [44]Department of Physics and Astronomy, University of Denver, Denver, CO 80208, USA. [45]Max-Planck Institut für Extraterrestrische Physik, 85748 Garching, Germany. [46]Institut für Astro- und Teilchenphysik and Institut für Theoretische Physik, Leopold-Franzens-Universität Innsbruck, A-6020 Innsbruck, Austria. [47]Space Sciences Division, NASA Ames Research Center, Moffett Field, CA 94035–1000, USA. [48]NYCB Real-Time Computing, Lattingtown, NY 11560–1025, USA. [49]Astronomical Observatory, Jagiellonian University, 30-244 Kraków, Poland. [50]Department of Chemistry and Physics, Purdue University Calumet, Hammond, IN 46323–2094, USA. [51]Institute of Space and Astronautical Science, Japanese Aerospace Exploration Agency, 3-1-1 Yoshinodai, Sagamihara, Kanagawa 229-8510, Japan. [52]Institució Catalana de Recerca i Estudis Avançats, Barcelona, Spain. [53]Consorzio Interuniversitario per la Fisica Spaziale, I-10133 Torino, Italy. [54]Dipartimento di Fisica, Università di Roma "Tor Vergata," I-00133 Roma, Italy. [55]School of Pure and Applied Natural Sciences, University of Kalmar, SE-391 82 Kalmar, Sweden. [56]Centre for Astrophysics Research, University of Hertfordshire, College Lane, Hatfield AL10 9AB, UK.

Supporting Online Material
www.sciencemag.org/cgi/content/full/science.1184656/DC1
Materials and Methods
SOM Text
Figs. S1 to S3
Tables S1 to S3
References

13 November 2009; accepted 19 March 2010
Published online 1 April 2010;
10.1126/science.1184656
Include this information when citing this paper.

The Equation of State of a Low-Temperature Fermi Gas with Tunable Interactions

N. Navon,*† S. Nascimbène,* F. Chevy, C. Salomon

Interacting fermions are ubiquitous in nature, and understanding their thermodynamics is an important problem. We measured the equation of state of a two-component ultracold Fermi gas for a wide range of interaction strengths at low temperature. A detailed comparison with theories including Monte-Carlo calculations and the Lee-Huang-Yang corrections for low-density bosonic and fermionic superfluids is presented. The low-temperature phase diagram of the spin-imbalanced gas reveals Fermi liquid behavior of the partially polarized normal phase for all but the weakest interactions. Our results provide a benchmark for many-body theories and are relevant to other fermionic systems such as the crust of neutron stars.

Recently, ultracold atomic Fermi gases have become a tool of choice to study strongly correlated quantum systems because of their high controllability, purity, and tunability of interactions (*1*). In the zero-range limit, interactions in a degenerate Fermi system with two spin-components are completely characterized by a single parameter $1/k_F a$, where a is the s-wave scattering length and $k_F = (6\pi^2 n)^{1/3}$ is the Fermi momentum (n is the density per spin state). In cold atom gases, the value of $|a|$ can be tuned over several orders of magnitude using a Feshbach resonance; this offers an opportunity to entirely explore the so-called BCS-BEC crossover, that is, the smooth transition from Bardeen-Cooper-Schrieffer (BCS) superfluidity at small negative values of a to molecular Bose-Einstein Condensation (BEC) at small positive values of a (*1*, *2*). Between these two well-understood limiting situations, a diverges, leading to strong quantum correlations. The description of this system is a challenge for many-body theories, as testified by the large amount of work in recent years (*1*). The physics of the BEC-BCS crossover is relevant for very different systems, ranging from neutron stars to heavy nuclei and superconductors.

Laboratoire Kastler Brossel, CNRS, Université Pierre et Marie Curie, École Normale Supérieure, 24 rue Lhomond, 75231 Paris, France.

*These authors contributed equally to this work.
†To whom correspondence should be addressed. E-mail: navon@ens.fr

In the grand-canonical ensemble and at zero temperature, dimensional analysis shows that the Equation of State (EoS) of a two-component Fermi gas, relating the pressure P to the chemical potentials μ_1 and μ_2 of the spin components can be written as

$$P(\mu_1,\mu_2,a) = P_0(\mu_1)h\left(\delta_1 \equiv \frac{\hbar}{\sqrt{2m\mu_1}a},\eta \equiv \frac{\mu_2}{\mu_1}\right) \qquad (1)$$

where $P_0(\mu_1) = 1/15\pi^2(2m/\hbar^2)^{3/2}\mu_1^{5/2}$ is the pressure of a single-component ideal Fermi gas, m is the atom mass, $\hbar$ is the Planck constant divided by 2π, and δ_1 is the grand-canonical analog of the dimensionless interaction parameter $1/k_F a$. The indices 1 and 2 refer to the majority and minority spin components, respectively. From the dimensionless function $h(\delta_1,\eta)$, it is possible to deduce all the thermodynamic properties of the gas, such as the compressibility, the magnetization, or the existence of phase transitions. The aim of this paper is to measure $h(\delta_1,\eta)$ for a range of interactions (δ_1) and spin imbalances (η) and discuss its physical content. Because it contains the same information as Eq. 1, the function h will also be referred to as the EoS in the rest of the text.

In situ absorption images of harmonically trapped gases are particularly suited to investigate the EoS, as first demonstrated in (*3*) and (*4*). In the particular case of the grand-canonical ensemble, a simple formula relates the local pressure P at a distance z from the center of the trap along the z axis to the doubly integrated density profiles $\bar{n}_1$ and $\bar{n}_2$ (*5*).

$$P(\mu_1(z),\mu_2(z),a) = \frac{m\omega_r^2}{2\pi}(\bar{n}_1(z) + \bar{n}_2(z)) \qquad (2)$$

Here, we define the local chemical potentials $\mu_i(z) = \mu_i^0 - \frac{1}{2}m\omega_z^2 z^2$, where μ_i^0 is the chemical potential of the component i at the bottom of the trap, assuming local density approximation. ω_r and ω_z are the transverse and axial angular frequencies of a cylindrically symmetric trap, respectively, and $\bar{n}_i(z) = \int n_i(x,y,z)\mathrm{d}x\mathrm{d}y$ is the atomic density n_i of the component i, doubly integrated over the transverse x and y directions. In a single experimental run at a given magnetic field, two images are recorded, providing $\bar{n}_1(z)$ and $\bar{n}_2(z)$ (fig. S4); the z-dependence of the chemical potentials then enables the measurement of P along a curve in the (δ_1,η) plane (*6*). This method was validated in (*4*) for the particular case of the